Omnidirectionally stretchable, biodegradable mesh electrode with re-entrant structure for spatial-stable functional position on dynamic organs

Jaewon Kim[1,2†], Kyung Su Kim[1,2†], Seungbin Kim[3], Yong-seok Lee[3]* and Jahyun Koo[1,2]*

[1]School of Biomedical Engineering, Korea University, Seongbuk-gu, Republic of Korea, [2]Interdisciplinary Program in Precision Public Health, Korea University, Seongbuk-gu, Republic of Korea, [3]Department of Mechanical Engineering, Myongji University, Yongin-si, Republic of Korea

The electrode, interfacing with soft tissue, is vulnerable to mechanical failure caused by dynamic organ motions such as cardiac activity, respiration, and digestion. Mechanical mismatch can also lead to tissue damage and sensor displacement. However, existing strategies for conformal integration often fall short of preserving mechanical compliance across large-area, multi-electrode arrays. Most internal organs undergo complex, anisotropic volumetric expansion from physiological activity, requiring implanted systems that can withstand multidirectional strains without inducing stress concentration. Conventional elastomers and mesh-structured electrodes typically exhibit a positive Poisson's ratio, which hinders multidirectional uniform stretching and results in mechanical mismatch at the tissue–electrode interface. This mismatch not only increases local mechanical load but also leads to electrode displacement. In this study, we propose a conformal electrode design that incorporates a re-entrant geometry into a stretchable and biodegradable polyurethane substrate. Mechanical testing confirmed that this geometry enhances stretchability and reduces the effective modulus of the electrode by approximately 64%. Furthermore, the device maintained electrical stability under cyclic deformation and preserved its structural integrity under dynamic, organ-mimicking volumetric expansion. This mechanical and electrical robustness highlights the potential of the proposed design for long-term integration into implantable electrode arrays for physiological monitoring and disease diagnosis on dynamic three-dimensional organ motion.

KEYWORDS

omnidirectional stretchability, biodegradable, re-entrant structure, 3D spatial stability, organ-conformal interface

1 Introduction

Implantable sensor systems have transformed physiological monitoring paradigms by enabling continuous, high-resolution detection of dynamic biological signals, including pressure (Kang et al., 2016; Shin et al., 2019), electrical activity (Koo et al., 2018; Maeng et al., 2022; Kim et al., 2023), and molecular markers (Liu et al., 2023; Hu et al., 2024). Clinical applications such as cardioverter-defibrillators for arrhythmia prevention (Goldberger and

Lampert, 2006; Maron et al., 2007), intracranial pressure monitors for brain injury management (Zhang et al., 2017; Nag et al., 2019), and urethral sensors for urinary incontinence (Majerus et al., 2017) highlight the versatility of implantable sensors in the field of biomedical engineering. However, despite their clinical success, these systems continue to face challenges caused by the dynamic physiological motion of tissue in long-term applications. Mechanical mismatches (Kozai et al., 2015; Wang et al., 2023), failure under mechanical stress (Jacobs et al., 2003; Ikar et al., 2020), and difficulty of achieving precise positioning and stable fixation of the sensor at the target site limit their long-term integration and functionality (Johnson et al., 1999; Ledet et al., 2012). These issues most frequently arise at the electrode component, which is in the closest contact with tissue. This highlights the necessity of developing electrodes that can maintain stable functionality while conforming intimately to the tissue.

Mechanical mismatches between device materials and soft tissues can lead to adverse biological responses. These mismatches include discrepancies in elastic modulus and Poisson's ratio. Most materials used in conventional implantable electrodes have a much higher elastic modulus, a characteristic of stiffness, compared to the surrounding tissue (Chen and Simmons, 2011). This can lead to chronic inflammation (Bedell et al., 2018), micromotion-induced damage (Dalrymple et al., 2025), and delamination at the interface (Kim et al., 2022). Furthermore, organs often undergo complex three-dimensional deformation and exhibit negative Poisson's ratio behavior. In contrast, most materials have a positive Poisson's ratio, making it difficult for them to accommodate organ deformation without exerting strain on the tissue (Chen et al., 2023; Kang et al., 2025). Such mechanical mismatches impede stable long-term integration and compromise both the functionality and biocompatibility of the implant. To overcome these mechanical limitations, there is a growing need for structural designs that enable otherwise rigid materials to conform mechanically to soft, dynamic biological environments (Lee et al., 2023; Bae et al., 2024). Among the various approaches, re-entrant architectures have attracted significant attention for their ability to induce system-level negative Poisson's ratio behavior by geometrically enabling lateral expansion under axial tension (Ni et al., 2024; Zhong et al., 2024). This geometry allows the implant to better conform to organ-level deformations and minimize interfacial stress. It also helps maintain stable long-term contact, closely mimicking the mechanics of native tissue (Fan et al., 2014; Su et al., 2017; Xia et al., 2022).

Beyond mechanical mismatch, the long-term persistence of conventional implants introduces an additional barrier to biocompatibility and clinical utility. Most clinically used materials are non-degradable, requiring surgical removal after temporary use and thereby increasing the risk of tissue damage, inflammation, and patient burden (Busam et al., 2006; Walley et al., 2017; Desai et al., 2024). Consequently, recent research has focused on biodegradable systems that safely degrade *in vivo* after fulfilling their diagnostic or therapeutic function (Acar et al., 2014; Huang et al., 2014; Hwang et al., 2015; Kang et al., 2015; Lu et al., 2019). Integrating biodegradability into implantable sensor systems provides a promising pathway toward safer, more patient-friendly devices, especially for transient applications in dynamic tissue

environments (Boutry et al., 2019; Lee et al., 2019; Choi et al., 2021; Lee et al., 2022; Zhang et al., 2025).

In this study, we fabricated the re-entrant structured electrode that achieves approximately 40% lower modulus than conventional materials and demonstrates improved conformability compared to other mesh-based designs. In addition, the electrode features a biodegradable polyurethane (PU) substrate, enabling temporary implantation and natural degradation after fulfilling its functional role. This design aims to address long-standing issues related to mechanical mismatch and instability at the tissue-device interface, fundamentally reducing inflammation and side effects during dynamic organ movement. The mechanical properties and behavior of the proposed electrodes were validated through mechanical testing and the finite element analysis (FEA). Systematic analysis with an expanding balloon model confirmed that the electrode minimized displacement, ensuring reliability of positional stable performance under dynamic volumetric deformation. These results highlight the potential of the electrode to maintain stable integration throughout its functional lifespan in mechanically dynamic biological environments.

2 Materials and methods

2.1 Electrode fabrication

To prepare the substrate, polycaprolactone (PCL) triol (PCL-triol; average Mn ~300/mol), hexamethylene diisocyanate (HDI), anhydrous butyl acetate, and tin (II) two-ethylhexanoate (Sn(Oct)$_2$) were obtained from Sigma-Aldrich. The synthesis began with melting 1.8 g of PCL-triol in a glass vial, followed by mixing HDI 1080 μL and butyl acetate 10 mL. Adding Sn(Oct)$_2$ as a catalyst 6.9 μL, followed by drop-casting on a hydrophobic surface treated with a self-assembled monolayer of trichloro (1H, 1H, 2H, 2H-perfluorooctyl) silane (Sigma-Aldrich). Substrates were placed for 24 h in an oven at 60 °C under vacuum condition for solvent evaporation and curing. We wash the sample using deionized water to remove potentially cytotoxic residual reagents. Details in synthesis of polycaprolactone-based bioresorbable PU were described in previous report (Choi et al., 2020).

A schematic illustration of the electrode fabrication process is provided in detail in Supplementary Figure S1. Molybdenum (Mo) foil (15 μm, Nilaco Co., Japan) attached on PU. It was ablated with an ultraviolet laser marker. To encapsulate the electrode using dynamic covalent networks structure for direct self-bonding, the two layers are strongly bonded using an uncured precursor and a process that involves hot pressing at 110 °C. It was ablated with an ultraviolet laser marker for cutting out the mesh pattern and the border of the electrode.

2.2 Tensile test

Tensile tests were conducted using a universal testing machine (Unitest M1, Testone, Korea). The test of polymer characteristics uses standard tensile specimens (ASTM-D412). And the tests of mesh structure where the load was applied at a constant speed of 1 mm/min until fracture occurred at room temperature. Strain is

defined as L/L_0, where L_0 and L are the length of the sample before and during elongation, respectively.

2.3 Cyclic tensile test

Customized mechanical testing system was exploited to evaluate the stability of electrodes under cyclic tensile loading which mimicking repetitive movement of biological tissues (10%, 20%, 30% strain). A photograph of the assembled system is presented in Supplementary Figure S2. The ending test also conducted on this system with a negative displacement setting up to 50% strain). The testing system had a linear actuator capable of applying sinusoidal tensile strain with programmable parameters such as displacement, frequency and acceleration using G-code. The resistance of metal trace consisting of electrodes was recorded by digital multimeter (BK Precision 880 LCR meter, BK Precision, United States).

2.4 Finite element analysis approach

Finite element analysis (FEA) was conducted using the software program ABAQUS/CAE 2022 (Simulia, United States). The generation of three-dimensional simulation models of re-entrant, square, and honeycomb structured electrodes was accomplished through the utilization of Fusion 360 software (Autodesk). In order to circumvent discrepancies in simulation outcomes attributable to variations in mesh density and element type, each FEA model was configured with the same element type, designated as C3D8R, and a global seed size of 0.2 mm. PU and Mo materials were applied to the FEA simulation. The elastic modulus of PU is 0.9 MPa (Choi et al., 2020), the Poisson's ratio is 0.45, and the elastic modulus of Mo is 330 GPa, the Poisson's ratio is 0.38 (Schulthess et al., 2023). It is important to note that all materials utilized in the simulation were assumed to be linear-elastic. The following three FEA simulations were conducted and Supplementary Figure S3 provides more details:

1. A tensile test simulation was conducted on each electrode-structured PU sample, with the samples undergoing a tensile strain ranging from 10% to 30% over the course of the experiment. The samples were subjected to a 10% strain increment.
2. A cyclic tensile test simulation was conducted on each structured molybdenum electrode, with a range of 10%–30% strain, and an interval of 10% was maintained throughout.
3. A displacement test was conducted using a balloon model simulation. In this test, Mo electrodes were stretched 5 mm in each direction along the x-axis. The translation degree of freedom along the z-axis was constrained to simulate the attachment of electrodes to the balloon. To mitigate the occurrence of rigid body motion, it was imperative to constrain all degrees of freedom.

2.5 3D displacement analysis using balloon model

To assess the mechanical adaptability of the fabricated mesh electrode during volumetric expansion, we conducted a displacement tracking experiment using a balloon model. The balloon was inflated and deflated using a syringe pump, which enabled precise and repeatable control over the volume of injected air. This approach ensured consistent deformation conditions across experiments.

The electrode was attached to the balloon at four points using epoxy. Marker points were placed at corresponding locations on both the electrode and the balloon surfaces. To assess the spatial relationship between the two layers during deformation, dual-camera imaging was employed.

Dual-camera imaging was used to record the electrode before and after expansion: one camera was aligned with the xz-plane, and the other was rotated 30° about the z-axis. Image analysis was performed using ImageJ to extract marker positions. To ensure the reproducibility of the balloon's deformation profile, video recordings were also analyzed to confirm that the balloon expanded and contracted into a nearly spherical shape.

Displacement vectors were calculated based on projections in both planes, assuming a shared z-axis. The electrode displacement was defined as the distance between the corresponding electrode and balloon markers following expansion.
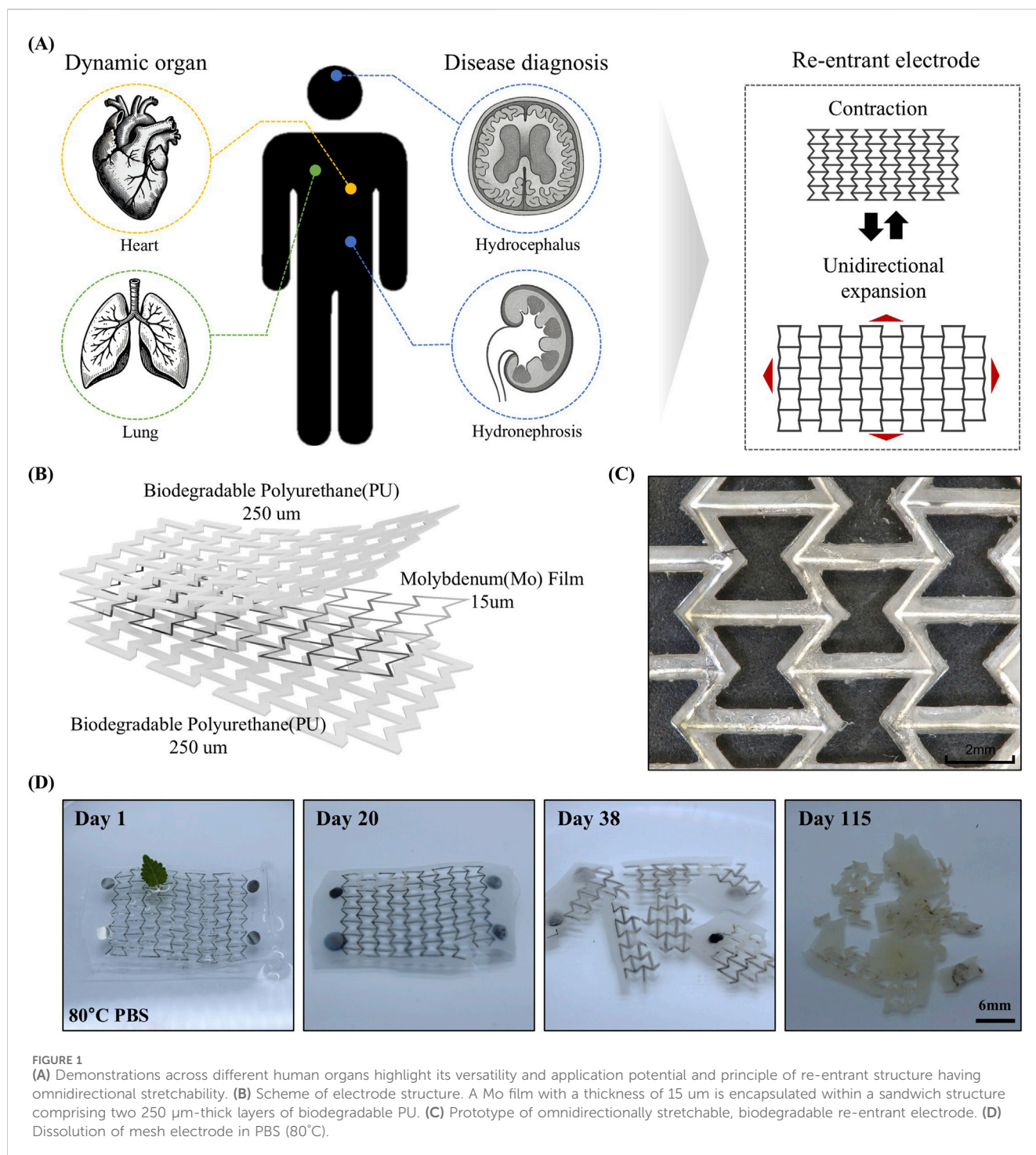
2.6 Biodegradation test

Re-entrant design mesh electrode is immersed in 0.1 M phosphate buffered saline (PBS) solution (Sigma-Aldrich) at 80°C. The sample was fully submerged to ensure uniform exposure to the degradation environment. The structural and morphological changes of the sample were periodically observed at specific time points. Optical images were captured using the digital camera (Canon EOS 600D, Japan) to document the progressive degradation of the polymeric matrix and electrode structure.

3 Results and discussion

3.1 Characteristics of electrode

Figure 1A presents a schematic representation of the potential applications of the proposed electrode. Negative Poisson's ratio of the re-entrant geometry enables the electrode to undergo isotropic expansion in all directions, similar to organ motion (Kang et al., 2025). Featuring a re-entrant geometry that exhibits a negative Poisson's ratio, the electrode can stretch easily in all directions under strain. This mechanical property allows the electrode to be applied directly onto organs in a patch form for physiological signal monitoring and diagnostics, or to be implanted after surgery for detecting disease recurrence. Furthermore, as the electrode is composed of biodegradable materials, it can naturally degrade and be absorbed by the body after a certain period of use, eliminating the need for secondary surgical removal. The structure of the electrode is displayed in Figure 1B. The device adopts a sandwich architecture. A biodegradable Mo film functions as the electrical conduction pathway and is embedded between layers

FIGURE 1
(A) Demonstrations across different human organs highlight its versatility and application potential and principle of re-entrant structure having omnidirectional stretchability. **(B)** Scheme of electrode structure. A Mo film with a thickness of 15 um is encapsulated within a sandwich structure comprising two 250 μm-thick layers of biodegradable PU. **(C)** Prototype of omnidirectionally stretchable, biodegradable re-entrant electrode. **(D)** Dissolution of mesh electrode in PBS (80°C).

of biodegradable PU substrates. Both PU and Mo used in the device have demonstrated long-term *in vitro* and *in vivo* biocompatibility in previous studies (Choi et al., 2020; Choi et al., 2022). Mo has been shown to degrade into molybdate ions under physiological conditions, which exhibit low cytotoxicity and induce only minimal local inflammatory response (Redlich et al., 2020; Redlich et al., 2021). Laser-based fabrication facilitates high-resolution patterning and the formation of narrow line widths, as clearly demonstrated in the optical microscopy image shown in Figure 1C.

Figure 1D shows the results of the accelerated dissolution test of the electrode in PBS at 80 °C. After 20 days, the PU encapsulation had swollen, and the Mo film began to oxidize and degrade. By day 38, the oxidation and degradation of both the Mo film and the PU layer had progressed significantly (Yin et al., 2014). After 118 days, most of the Mo had fully degraded, accompanied by surface erosion of the polymer, resulting in increased opacity. According to Arrhenius equations, it represents all the materials can degrade 590 days in physiological temperature (37 °C) (Choi et al., 2020).
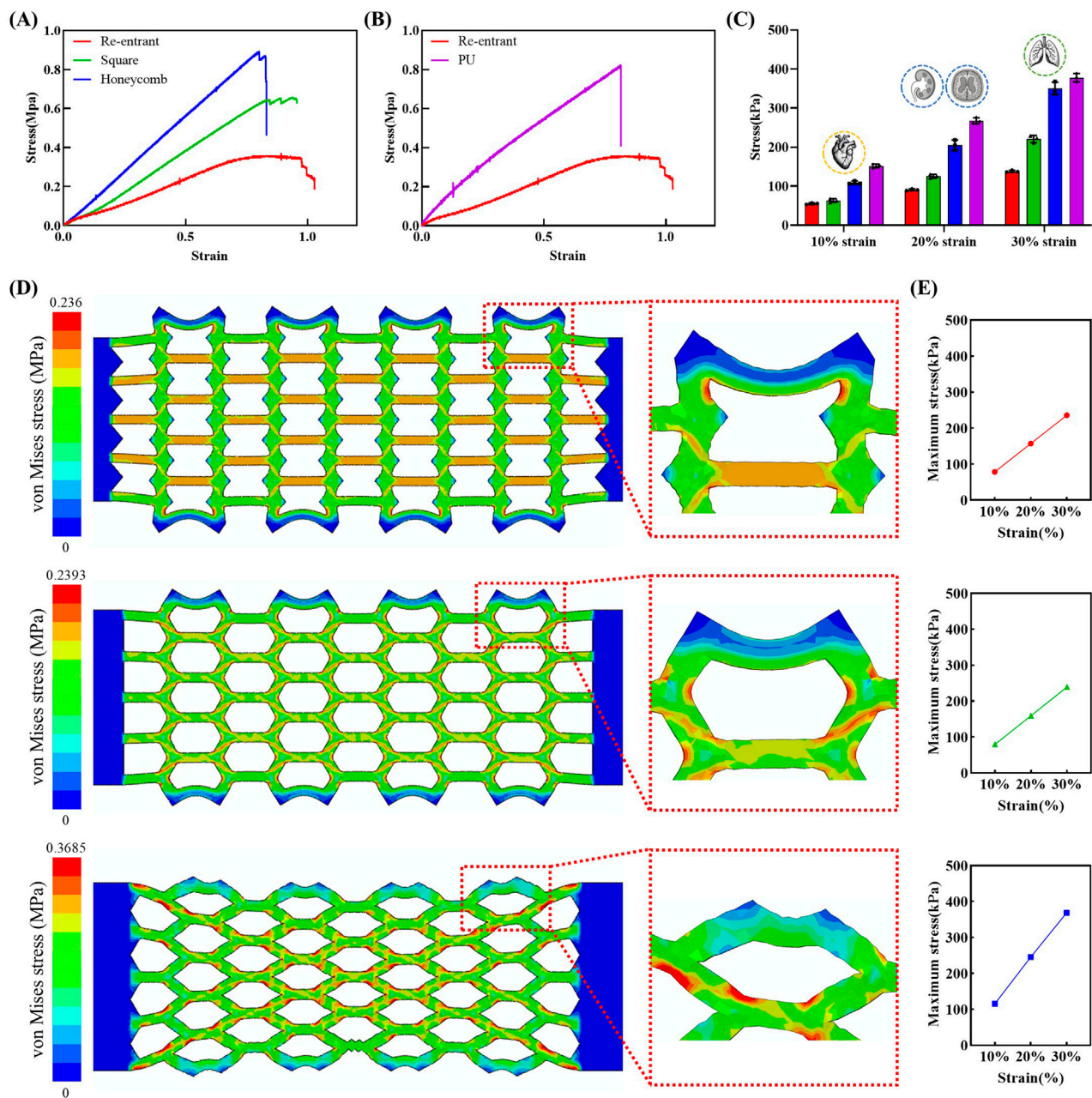
FIGURE 2
Tensile stress-strain curves and corresponding stress values at specific strain levels (10%, 20%, 30%) for various structural designs and materials. **(A)** Comparison of stress-strain responses of re-entrant, square, and honeycomb structures. **(B)** Stress-strain curves of re-entrant structure and biodegradable PU film. **(C)** Stress values at selected strain levels for mesh structures and PU film (n = 3 per groups). Each bar represents the average stress value, and the error bars indicate the standard deviation. **(D)** Von-Mises stress contours in FEA results of re-entrant, square, and honeycomb structures for 30% tension. **(E)** Maximum von- Mises stress in FEA results of re-entrant, square, and honeycomb structures for each 10%, 20%, 30% tension.

3.2 Tensile characteristics of mesh structure

Soft tissues exhibit Young's moduli (E) in the range of 100 Pa to 10 MPa, highlighting the importance of mechanical compatibility for successful integration (Fallegger et al., 2020). Most soft tissues, excluding bone, possess moduli in the tens of kilopascals range (Guimarães et al., 2020). This mechanical softness poses a challenge to achieving mechanical matching, as conventional polymeric materials typically exhibit moduli in

the megapascal range (Qian and Zhao, 2018). Simultaneously, sufficient stretchability is also essential to ensure seamless integration with highly dynamic organs (Geraghty et al., 2004; Hostettler et al., 2010). Figure 2A presents the tensile test results of the mesh-structured polymer. To enable a comparative analysis of mesh designs, three distinct structural types were prepared: re-entrant, offset rectangle, and honeycomb (Okumura et al., 2021). The results demonstrate that, among the three mesh geometries tested, the re-entrant structure exhibits the lowest

Young's modulus and the highest stretchability. Figure 2B illustrates the comparative mechanical data between the re-entrant structure and the bulk polymer material. In addition to comparisons with other mesh geometries, the re-entrant structure demonstrates a significantly lower Young's modulus and greater strain capacity relative to the bulk polymer. These findings indicate that employing mesh architecture, particularly the re-entrant design, can effectively mitigate mechanical mismatches with soft tissues. Moreover, this structural strategy alone is sufficient to enable the development of electrodes that are not only soft and stretchable but also reliable in mechanically active biological environments. The enhanced mechanical compliance of the re-entrant structure suggests its potential suitability for integration with tissues undergoing frequent volumetric changes.

Given that human organs undergo repeated cycles of volumetric change, comparing stress values at specific strain levels is critical for assessing mechanical compatibility. Figure 2C presents a summary of the stress values corresponding to 10%, 20%, and 30% strain for each structural design and bulk material. At 10% strain, the re-entrant structure shows a remarkably low stress value of 53 kPa, increasing to 88 kPa at 20% and 135 kPa at 30%. Although the strains assessed in this study were measured under uniaxial (1D) conditions, the resulting stress values are relevant to the mechanical deformation observed during three-dimensional organ motion. Notably, the 10%, 20%, and 30% strain levels correspond to the typical deformation ranges encountered in the heart (Carlsson et al., 2004; Aguado-Sierra et al., 2011), organs affected by swelling-related diseases such as hydrocephalus and hydronephrosis (Riccabona et al., 2005; Wang et al., 2019; Holmgren et al., 2025), and the lungs (Plathow et al., 2004; Swift et al., 2007; Miyawaki et al., 2016), respectively. The strain levels for the heart and lungs were estimated based on reported changes in sagittal length during physiological motion. The strain levels for hydrocephalus and hydronephrosis were inferred separately by converting reported volumetric expansions into corresponding linear deformations. This approach enabled a consistent estimation of strain across organs with differing deformation characteristics.

Figure 2D presents the von-Mises stress contours in FEA results of the tensile test simulation. It was confirmed that when electrodes were stretched to 30% of their original length, all structures exhibited a stress distribution of 100–200 kPa throughout the entire domain. Furthermore, elevated levels of stress were detected in proximity to the connection region of each unit electrode configuration. Local high stress regions are delineated in Figure 2D, indicated by red coloration in the FEA contour results. These regions may be considered at risk of failure. Honeycomb and square structures exhibit higher levels of stress concentration compared to re-entrant structures, with the magnitude of stress being also greater in the former. As demonstrated in Figure 2E, the maximum von-Mises stress increase for the re-entrant and square structures was less pronounced than that of the honeycomb structure. The re-entrant structure demonstrated the lowest maximum von-Mises stress, with values of 78.6, 157.6, and 236 kPa at 10%, 20%, and 30% strain levels, respectively. The resultant value at 30% strain is 35% lower than that of the honeycomb structure.

3.3 Electrical stability of mesh structure electrode

When the electrode serves as structural support for sensor system integration or functions as a strain sensor, it is exposed to mechanical deformations. These deformations include changes in strain and bending curvature. These deformations can significantly alter the electrical resistance of the electrode. This variation in resistance may degrade sensing performance, hinder accurate disease diagnosis, and ultimately reduce the operational lifespan of the sensor. Furthermore, exposure to large cyclic strains can induce microcrack formation in the metal-based electrode, compromising its electrical integrity (Chen et al., 1995; Kim et al., 2013; Bag et al., 2017; Mohammed, 2024). These variations in resistance compromise both the operational stability of the sensor system and the intrinsic reliability of the electrode.

As shown in Figure 3A, during organ volumetric expansion, the strain applied to the electrode increases while the bending radius decreases. Conversely, during organ contraction, the applied strain decreases and the bending radius increases. Figure 3B presents the experimental results of resistance variation in response to applied strain measuring relative resistance change ($\Delta R/R_0$) under applied strain levels of up to 30%. The re-entrant structure demonstrated negligible resistance change across the applied strain range. Similarly, the square structure also exhibited negligible resistance change under applied strain. In contrast, the honeycomb structure showed mechanical failure, including electrode rupture at 30% strain. This phenomenon is further illustrated in Figure 3C, which shows photographs depicting the morphological changes of each mesh structure under varying strain levels. The re-entrant structure exhibits notably less morphological deformation compared to the other configurations, as highlighted by the red boxes and arrows. The minimal displacement observed in the mesh electrode played a critical role in maintaining its structural and functional stability under mechanical strain.

Figure 3D shows the relative resistance change ($\Delta R/R_0$) of mesh electrode structures under varying bending radii. As the bending radius decreased, all structures consistently exhibited minimal resistance variation, indicating excellent electrical stability even under substantial mechanical deformation. This electrical stability is further supported by side-view images in Figure 3E. Throughout the bending process, the re-entrant and square structures exhibited negligible morphological deformation. Similarly, the honeycomb structure maintained its geometry without observable tearing or mechanical failure. This behavior is attributed to the inherent flexibility of the thin metal film. Detailed information regarding the corresponding bending deformation for each result is provided in Supplementary Figure S4.

Figure 4 presents the assessment of structural and electrical stability under cyclic strain conditions. The parameters used in this experiment were designed to mimic the mechanical conditions of human organs, as illustrated in Figure 4A. A 10% strain was applied to simulate cardiac motion. The strain rate was set between 80 and 100 bpm, reflecting the typical human heart rate. In addition, strains of 20% and 30% were applied to mimic normal and deep respiratory motions, respectively (Arakawa et al., 2000). The corresponding strain rates were chosen within the typical human respiratory rate range of 10–20 bpm.
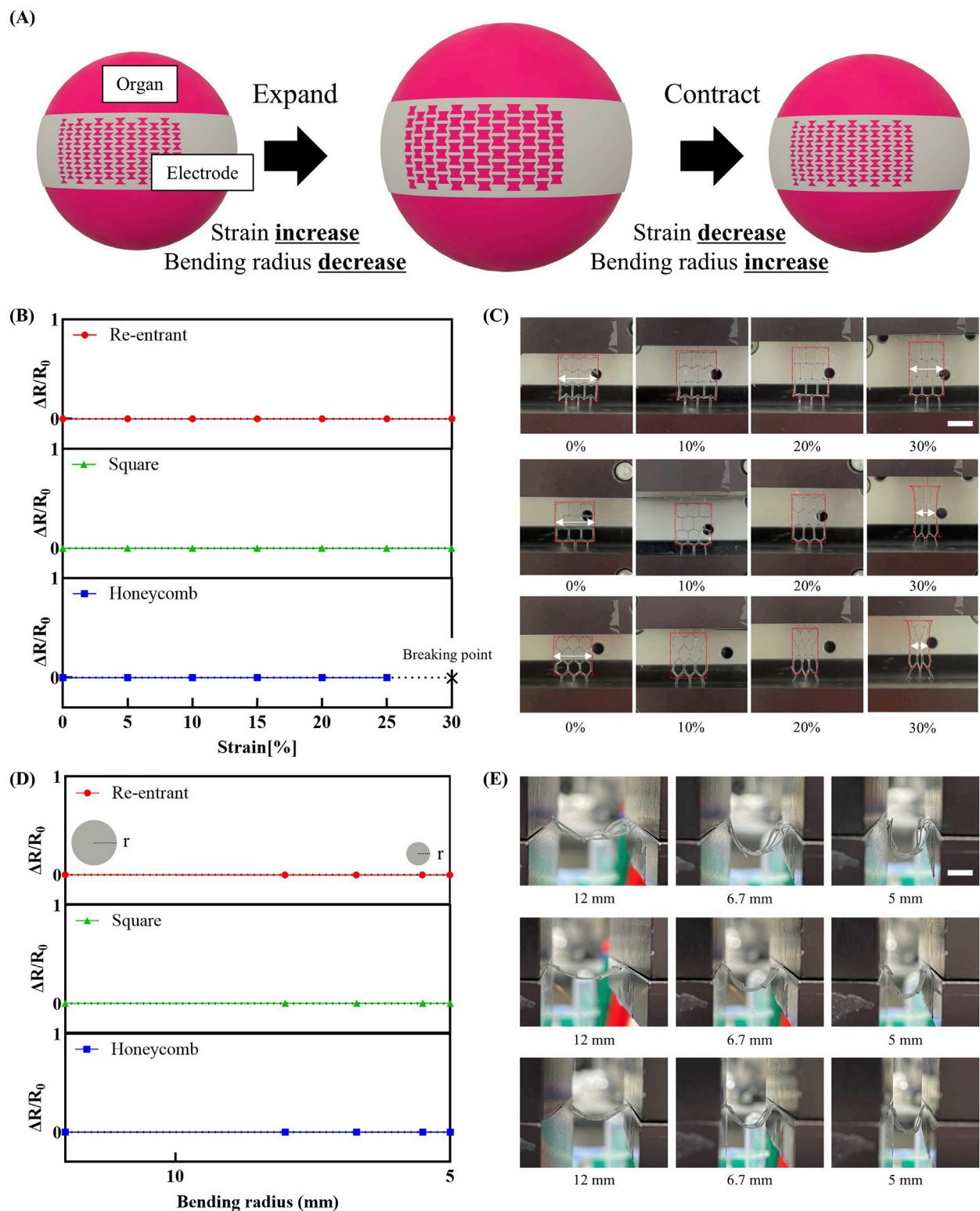
FIGURE 3
Variation of electrode resistance with mechanical strain. **(A)** Schematic representation of variations in strain and bending modulus in an organ undergoing three-dimensional volumetric changes. **(B)** Change in relative resistance change (AR/Ro) as a function of applied strain (n = 3 per groups). Each point represents the average AR/Ro value, and the error bars indicate the standard deviation. **(C)** Photographs showing morphological changes of each mesh structure under varying strain (scale bar: 16 mm). **(D)** Change in AR/Ro as a function of bending radius (n = 3 per groups). Each point represents the average AR/Ro value, and the error bars indicate the standard deviation. **(E)** Photographs showing morphological changes of each mesh structure under varying bending modulus (scale bar: 8 mm).
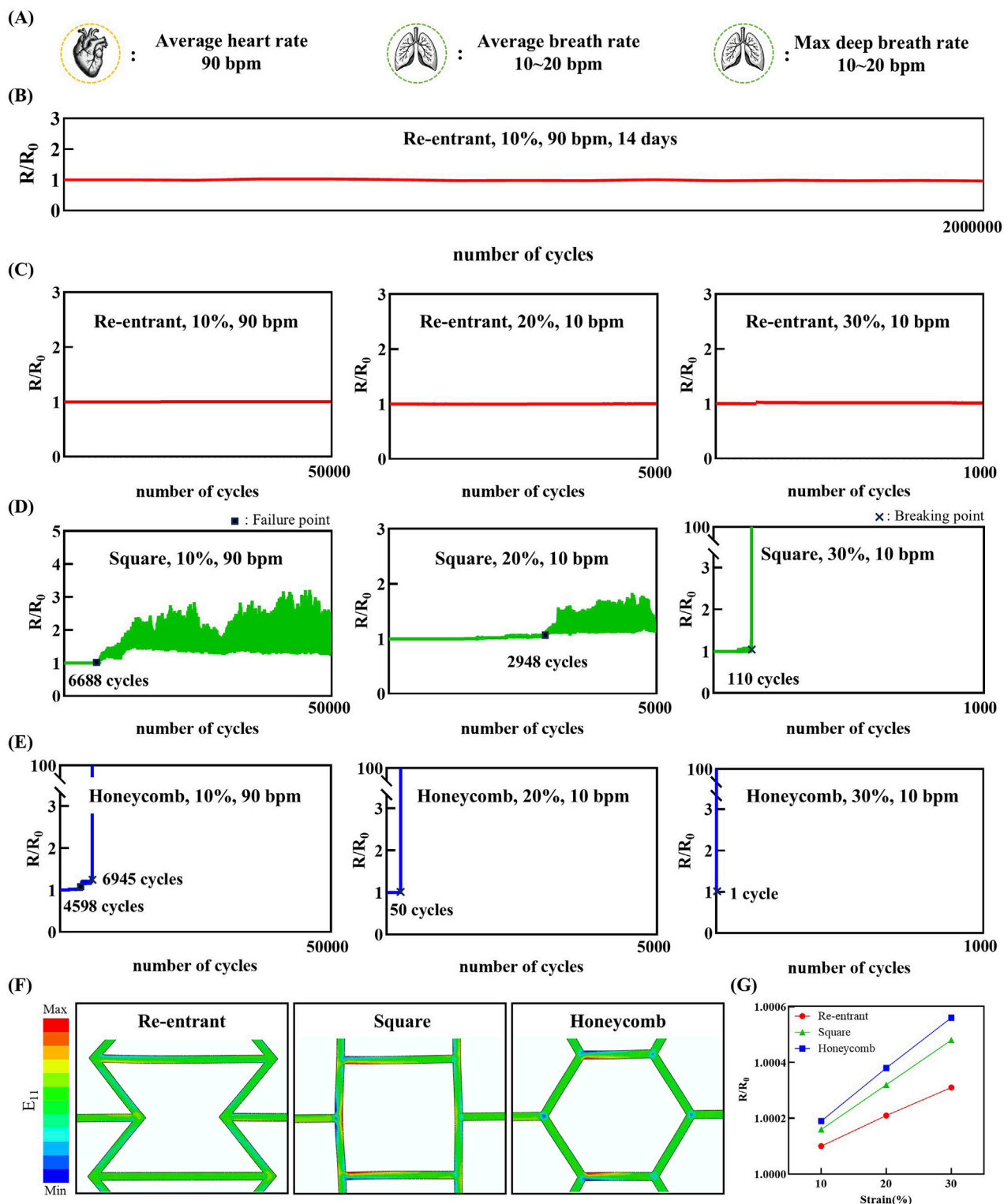
FIGURE 4
Relative resistance change (R/R$_0$) of the sensor under cyclic strain loading, demonstrating stable and repeatable electrical response over multiple deformation cycles. **(A)** Physiologically relevant cycle rates representing cardiac (90 bpm) and respiratory (10 bpm) rate. **(B)** Relative resistance change of the re-entrant structure under 10% cyclic strain at 90 bpm for 14 days. **(C–E)** Experimental results of electrodes with a re-entrant, square, honeycomb structure, respectively. **(F)** Strain (E11) contours in FEA results of re-entrant, square, and honeycomb structure unit cells for 30% tension. **(G)** Relative resistance change results of re-entrant, square, and honeycomb structures for each 10%, 20%, 30% tension.

Figure 4B demonstrates the long-term stability of the re-entrant structure. Under simulated physiological motion of 10% cyclic strain at 90 bpm, the electrode maintained both structural and electrical integrity for over 14 days without any observable damage. This duration aligns with the intended operational period of biodegradable electrodes, typically designed for approximately 2 weeks of *in vivo* use (Tsang et al., 2015; Park et al., 2024). Figure 4C presents the performance of the re-entrant structure under the defined cyclic strain conditions. The experimental results demonstrate that the re-entrant structure exhibits excellent electrical stability, showing minimal changes in resistance under repeated strain conditions of 10% for 50,000 cycles, 20% for 5,000 cycles, and 30% for 1,000 cycles. Figure 4D illustrates the performance of the square structure under the same conditions. By contrast, the square structure exhibited electrical instability after 6,688 cycles under 10% cyclic strain. Similarly, under 20% strain, resistance instability occurred after 2,948 cycles. These were designated as failure points, indicating that while microcracks affected resistance, complete electrical disconnection did not occur. Under 30% strain, complete electrical failure occurred after only 110 cycles, marked as the breaking point. Figure 4E illustrates the performance of the honeycomb structure under the same conditions. The honeycomb structure exhibited failure after 4,598 cycles under 10% cyclic strain, followed by complete electrical breaking at 6,945 cycles. Under 20% strain, electrical breaking occurred after only 50 cycles. At 30% strain, mechanical fracture occurred even before the completion of a single cycle. These findings are consistent with the morphological observations shown in Figure 3C.

The strain contour result of the cyclic tensile test FEA simulation is shown in Figure 4F. The strain of the material itself has a dominant effect on the resistance change of the electrode rather than the structural deformation of the structured electrode. In a manner analogous to the tensile test FEA simulation, the re-entrant structure exhibited a reduced deformation of the element itself in comparison to the other structured electrodes. The findings of the FEA reveal a discrepancy in the deformation mitigation capabilities of the re-entrant, honeycomb, and square structured electrodes when compared to their counterparts. Specifically, the electrodes demonstrate an inability to effectively mitigate deformation along the x-axis direction. The strain components were extracted to calculate the relative resistance change of each electrode. In the context of the present study, the FEA simulation was configured to stretch the electrode once. However, if the electrode is subjected to a fatigue load environment with a stress ratio greater than or equal to zero, as is the case in the conducted test environment discussed in this article, the material will deform in the direction of increasing E11 and decreasing E22 and E33, a phenomenon that can be attributed to the Poisson effect. Consequently, the relative resistance change result trend may persist despite an increase in the number of cycles. As illustrated in Figure 4G, for the re-entrant and honeycomb electrode, strain along the x-axis direction was observed to occur at the 10% strain level, with values of 0.55% and 1%, respectively. Correspondingly, the relative resistance change values were 1.0001 and 1.00019, respectively. The re-entrant electrode exhibited a comparatively diminished relative resistance change, registering at 1.66% of strain at the 30% strain level, as compared to the honeycomb electrode.

These results indicate that all three mesh structures provide a certain level of mechanical flexibility and electrical stability. Among the three structures, the re-entrant design demonstrates superior structural robustness. It exhibits enhanced performance under conditions involving repeated volumetric deformation, outperforming the other mesh configurations. This superior performance highlights the potential of the re-entrant structure for applications requiring long-term mechanical reliability.

3.4 Analysis of structural stability under 3D morphological changes

Under physiological conditions, internal organs are constantly subjected to dynamic mechanical environments due to intrinsic motions such as respiration, heartbeat, and peristalsis, as well as external mechanical influences (Leucht et al., 2007; Elsayed, 2019; Wang et al., 2021; Wang et al., 2025). These dynamic environments not only affect the mechanical durability of implantable electrodes but also pose significant challenges for maintaining positional stability, which is critical for accurate sensing performance (Markodimitraki et al., 2022; Abad-Coronel et al., 2024). While spatial fixation is essential, previous validation efforts have predominantly focused on simplified planar or uniaxial motion (Chen et al., 2020; Chen et al., 2021). However, biological tissues undergo complex three-dimensional volumetric deformation, highlighting the need for an evaluation strategy that reflects these physiologically relevant dynamics (Morikawa et al., 2019; Kim et al., 2024). To address this, we developed an alternative assessment method using a spherically inflating balloon to simulate organ-like volumetric expansion and contraction. An electrode was mounted on the balloon surface, enabling analysis of the relative displacement between the dynamic tissue-mimicking surface and the electrode during deformation.

Figure 5A presents images capturing the morphological evolution of the electrode during volumetric expansion. These observations underscore a key mechanism by which the re-entrant electrode maintains positional stability. Owing to its geometry-induced negative Poisson's ratio, the re-entrant structure undergoes simultaneous expansion in both horizontal and vertical directions when uniaxial strain is applied. This omnidirectional deformation allows the electrode to conform to organ-like volumetric changes, thereby preserving stable contact during dynamic motion.

As illustrated in Figure 5B, the displacement result is presented along the y-axis direction of the displacement test using balloon model simulation. Electrode designs, including re-entrant and honeycomb structures, exhibited displacements ranging from 2 to 4 mm in regions distant from the x-axis. In contrast, the square-structured electrode demonstrated a maximum displacement of approximately 2 mm. The upper region, situated at a considerable distance from the x-axis, is indicated in blue, while the lower region, located at a greater distance from the x-axis, is highlighted in red. It can be inferred that the electrode would undergo a contraction when subjected to stretching along the x-axis. Conversely, the electrode would undergo an expansion when stretched along the x-axis, with the respective colors denoting this behavior in each region. Consequently, the re-
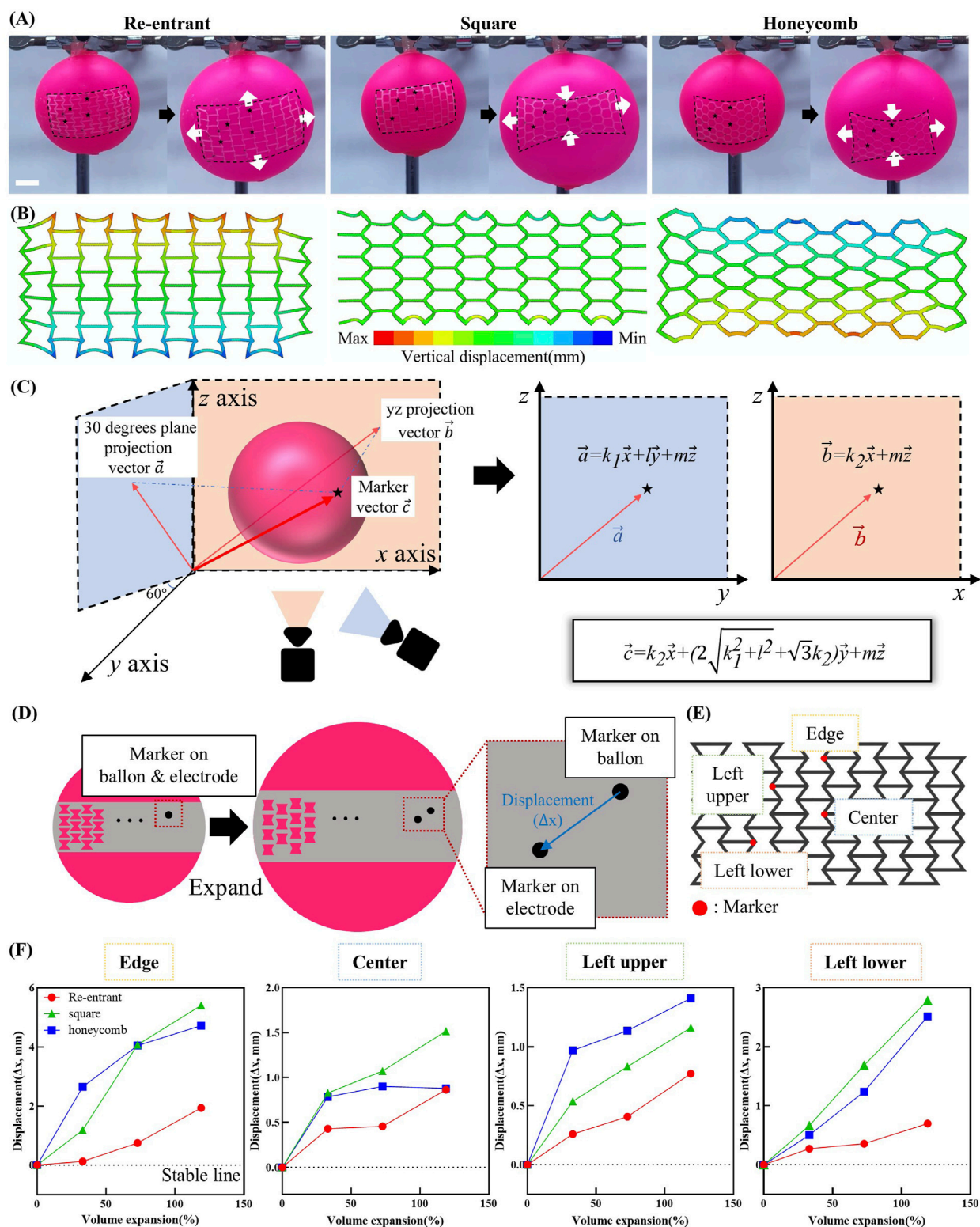
FIGURE 5
Morphological stability test under organ-inspired 3D deformation. **(A)** Photographs showing the deformations of the re-entrant, square and honeycomb shaped electrode while increasing the balloon volume. Arrows indicate the direction of electrode elongation. **(B)** Displacement (U2) contour in FEA results of re-entrant, square, and honeycomb structures for a simplified balloon test simulation. **(C)** Schematic illustration of the method for calculating 3D vectors of markers on the balloon surface. **(D)** Schematic illustration of the displacement mechanism between markers on balloon and markers on electrode during 3D volumetric expansion. **(E)** Schematic showing the placement of markers on the electrode. **(F)** Quantified displacement of individual points under volumetric deformation.

entrant structured electrode exhibited a displacement trend analogous to that of organic tissue, demonstrating positive displacement in all directions. In contrast, the honeycomb and square structured electrodes caused damage to the tissue due to its shrinkage along the y-axis direction.

Figure 5C outlines the computational approach used to extract the position vectors of marker points placed on both the electrode and the balloon based on recorded video data. The video provides two projections: one onto the xz-plane and another onto a plane rotated 30° around the z-axis. As the projected vectors share a common z-axis, the x and y positions can be calculated by combining total length and angular information obtained through image analysis. These computed coordinates are then used to reconstruct the full 3D spatial position vectors of the markers. A detailed step-by-step procedure is provided in Supplementary Figure S5.

The principle used to quantify electrode stability based on the calculated position vectors is illustrated in Figure 5D. Markers were initially aligned on the balloon and electrode surfaces in the unexpanded state. Upon inflation, differential deformation increased the distance between corresponding markers, allowing displacement to be calculated from the reconstructed position vectors. These vectors were obtained through analysis of the recorded video images.

Figure 5E displays the marker placement strategy. Within each unit cell of the mesh structure, markers were positioned at regions predicted to exhibit the greatest deformation. Additional markers were placed at the top, center, and near the upper and lower edges of the electrode to capture position-dependent responses. Morphological changes during volumetric expansion are detailed in Supplementary Figure S6. Figure 5F summarizes the displacement results corresponding to volume expansions of approximately 33%, 73%, and 118%, calculated from the measured radii of the inflated balloon. Across all expansion levels and measurement points, the re-entrant structure consistently exhibited the smallest displacements and the highest spatial uniformity. At 33% and 73% volume expansion, the displacement ranges were minimal at 0.31 mm and 0.39 mm, respectively. This result demonstrates a uniformly distributed mechanical response. Even at 118% volume expansion, the range remained comparatively low at 1.24 mm, substantially smaller than those observed in the square (4.25 mm) and honeycomb (3.84 mm) structures. This uniform deformation under dynamic volumetric expansion enhances positional stability and minimizes localized mechanical stress. Such mechanical advantage improves the reliability of sensor readings in implantable systems, particularly where internal structural monitoring is not feasible.

To demonstrate the functional applicability of the re-entrant electrode beyond mechanical and electrical stability, we designed a wireless power transfer experiment in which the electrode served as a receiving antenna. The fabricated coil with a re-entrant structure was connected to a surface-mounted LED and placed in proximity to a transmitting (T_x) antenna. Upon excitation at a resonant frequency of 32.4 MHz, the LED was successfully powered wirelessly, as shown in Supplementary Figure S7. This result confirms the feasibility of utilizing the re-entrant electrode as a flexible antenna for wireless energy harvesting and power delivery applications.

4 Conclusion

In this study, a re-entrant geometry was incorporated into a biodegradable polymer-based electrode to improve mechanical conformity and biocompatibility with soft tissues. Experimental evaluation confirmed that the re-entrant structure effectively reduces the modulus experienced by the electrode, thereby minimizing mechanical mismatch with surrounding soft tissues. In parallel, the electrode maintained stable electrical performance under repeated deformations that mimic dynamic organ motion. Simulations further validated the mechanical behavior, supporting the robustness and consistency of the experimental findings. Additionally, through a balloon-based volumetric deformation model, the electrode demonstrated superior positional stability under dynamic expansion. These findings suggest that the proposed electrode design holds significant potential for future integration into implantable devices, such as electrode arrays, for continuous physiological signal monitoring and diagnosis of disease progression or recurrence. Importantly, the re-entrant mesh architecture can be readily adapted to a wide range of stretchable polymer systems. This architecture-driven strategy provides a structurally versatile framework for engineering mechanically compliant bioelectronic interfaces across various implantable systems.

Data availability statement

The raw data supporting the conclusions of this article will be made available by the authors, without undue reservation.

Author contributions

JeK: Data curation, Visualization, Investigation, Formal Analysis, Writing – review and editing, Writing – original draft. KK: Conceptualization, Methodology, Writing – review and editing. SK: Formal Analysis, Visualization, Investigation, Writing – review and editing. Y-sL: Supervision, Methodology, Writing – review and editing. JhK: Project administration, Supervision, Methodology, Writing – review and editing, Funding acquisition, Resources.

Funding

Conflict of interest

The authors declare that the research was conducted in the absence of any commercial or financial relationships that could be construed as a potential conflict of interest.

Generative AI statement

The author(s) declare that no Generative AI was used in the creation of this manuscript.

Publisher's note

All claims expressed in this article are solely those of the authors and do not necessarily represent those of their affiliated organizations, or those of the publisher, the editors and the reviewers. Any product that may be evaluated in this article, or claim that may be made by its manufacturer, is not guaranteed or endorsed by the publisher.

Supplementary material

The Supplementary Material for this article can be found online at: https://www.frontiersin.org/articles/10.3389/fnano.2025.1634033/full#supplementary-material

References

Abad-Coronel, C., Vandeweghe, S., Cervantes, M. D. V., Lara, M. J. T., Cordova, N. M., and Aliaga, P. (2024). Accuracy of implant placement using digital prosthetically-derived surgical guides: a systematic review. *Appl. Sci.* 14 (16), 7422. doi:10.3390/app14167422

Acar, H., Çinar, S., Thunga, M., Kessler, M. R., Hashemi, N., and Montazami, R. (2014). Study of physically transient insulating materials as a potential platform for transient electronics and bioelectronics. *Adv. Funct. Mater.* 24 (26), 4135–4143. doi:10.1002/adfm.201304186

Aguado-Sierra, J., Krishnamurthy, A., Villongco, C., Chuang, J., Howard, E., Gonzales, M. J., et al. (2011). Patient-specific modeling of dyssynchronous heart failure: a case study. *Prog. biophysics Mol. Biol.* 107 (1), 147–155. doi:10.1016/j.pbiomolbio.2011.06.014

Arakawa, H., Niimi, H., Kurihara, Y., Nakajima, Y., and Webb, W. R. (2000). Expiratory high-resolution CT: diagnostic value in diffuse lung diseases. *Am. J. Roentgenol.* 175 (6), 1537–1543. doi:10.2214/ajr.175.6.1751537

Bae, J. Y., Hwang, G. S., Kim, Y. S., Jeon, J., Chae, M., Kim, J. W., et al. (2024). A biodegradable and self-deployable electronic tent electrode for brain cortex interfacing. *Nat. Electron.* 7 (9), 815–828. doi:10.1038/s41928-024-01216-x

Bag, A., Park, K. S., and Choi, S. H. (2017). Effects of microcrack evolution on the electrical resistance of Cu thin films on flexible PI substrates during cyclic-bend testing. *Metals Mater. Int.* 23 (4), 673–682. doi:10.1007/s12540-017-6735-4

Bedell, H. W., Song, S., Li, X., Molinich, E., Lin, S., Stiller, A., et al. (2018). Understanding the effects of both CD14-mediated innate immunity and device/tissue mechanical mismatch in the neuroinflammatory response to intracortical microelectrodes. *Front. Neurosci.* 12, 772. doi:10.3389/fnins.2018.00772

Boutry, C. M., Beker, L., Kaizawa, Y., Vassos, C., Tran, H., Hinckley, A. C., et al. (2019). Biodegradable and flexible arterial-pulse sensor for the wireless monitoring of blood flow. *Nat. Biomed. Eng.* 3 (1), 47–57. doi:10.1038/s41551-018-0336-5

Busam, M. L., Esther, R. J., and Obremskey, W. T. (2006). Hardware removal: indications and expectations. *JAAOS-Journal Am. Acad. Orthop. Surg.* 14 (2), 113–120. doi:10.5435/00124635-200602000-00006

Carlsson, M., Cain, P., Holmqvist, C., Stahlberg, F., Lundback, S., and Arheden, H. (2004). Total heart volume variation throughout the cardiac cycle in humans. *Am. J. Physiology-Heart Circulatory Physiology* 287 (1), H243–H250. doi:10.1152/ajpheart.01125.2003

Chen, E. Y., Lawson, L., and Meshii, M. (1995). The effect of fatigue microcracks on rapid catastrophic failure in Al-SiC composites. *Mater. Sci. Eng. a-Structural Mater. Prop. Microstruct. Process.* 200 (1-2), 192–206. doi:10.1016/0921-5093(95)07009-5

Chen, K., Ren, J. Y., Chen, C. Y., Xu, W., and Zhang, S. (2020). Safety and effectiveness evaluation of flexible electronic materials for next generation wearable and implantable medical devices. *Nano Today* 35, 100939. doi:10.1016/j.nantod.2020.100939

Chen, M. X., Wang, Z., Li, K. W., Wang, X. D., and Wei, L. (2021). Elastic and stretchable functional fibers: a review of materials, fabrication methods, and applications. *Adv. Fiber Mater.* 3 (1), 1–13. doi:10.1007/s42765-020-00057-5

Chen, W. L., and Simmons, C. A. (2011). Lessons from (patho)physiological tissue stiffness and their implications for drug screening, drug delivery and regenerative medicine. *Adv. Drug Deliv. Rev.* 63 (4-5), 269–276. doi:10.1016/j.addr.2011.01.004

Chen, Y., Zhou, Y., Hu, Z., Lu, W., Li, Z., Gao, N., et al. (2023). Gelatin-based metamaterial hydrogel films with high conformality for ultra-soft tissue monitoring. *Nanomicro Lett.* 16 (1), 34. doi:10.1007/s40820-023-01225-z

Choi, Y. S., Hsueh, Y. Y., Koo, J., Yang, Q., Avila, R., Hu, B., et al. (2020). Stretchable, dynamic covalent polymers for soft, long-lived bioresorbable electronic stimulators designed to facilitate neuromuscular regeneration. *Nat. Commun.* 11 (1), 5990. doi:10.1038/s41467-020-19660-6

Choi, Y. S., Jeong, H., Yin, R. T., Avila, R., Pfenniger, A., Yoo, J., et al. (2022). A transient, closed-loop network of wireless, body-integrated devices for autonomous electrotherapy. *Science* 376 (6596), 1006–1012. doi:10.1126/science.abm1703

Choi, Y. S., Yin, R. T., Pfenniger, A., Koo, J., Avila, R., Benjamin Lee, K., et al. (2021). Fully implantable and bioresorbable cardiac pacemakers without leads or batteries. *Nat. Biotechnol.* 39 (10), 1228–1238. doi:10.1038/s41587-021-00948-x

Dalrymple, A. N., Jones, S. T., Fallon, J. B., Shepherd, R. K., and Weber, D. J. (2025). Overcoming failure: improving acceptance and success of implanted neural interfaces. *Bioelectron. Med.* 11 (1), 6. doi:10.1186/s42234-025-00168-7

Desai, V. M., Mahon, S. J., Pang, A., Hauth, L., Shah, A. S., and Anari, J. B. (2024). Complications of hardware removal in pediatric orthopaedic surgery. *J. Pediatr. Orthop.* 44 (10), e957–e964. doi:10.1097/BPO.0000000000002780

Elsayed, M. D. (2019). Biomechanical factors that influence the bone-implant-interface. *Res. Rep. Oral Maxillofac. Surg.* 3 (1), 1–14. doi:10.23937/2643-3907/1710023

Fallegger, F., Schiavone, G., and Lacour, S. P. (2020). Conformable hybrid systems for implantable bioelectronic interfaces. *Adv. Mater.* 32 (15), e1903904. doi:10.1002/adma.201903904

Fan, J. A., Yeo, W. H., Su, Y., Hattori, Y., Lee, W., Jung, S. Y., et al. (2014). Fractal design concepts for stretchable electronics. *Nat. Commun.* 5 (1), 3266. doi:10.1038/ncomms4266

Geraghty, E. M., Boone, J. M., McGahan, J. P., and Jain, K. (2004). Normal organ volume assessment from abdominal CT. *Abdom. imaging* 29 (4), 482–490. doi:10.1007/s00261-003-0139-2

Goldberger, Z., and Lampert, R. (2006). Implantable cardioverter-defibrillators: expanding indications and technologies. *Jama* 295 (7), 809–818. doi:10.1001/jama.295.7.809

Guimarães, C. F., Gasperini, L., Marques, A. P., and Reis, R. L. (2020). The stiffness of living tissues and its implications for tissue engineering. *Nat. Rev. Mater.* 5 (5), 351–370. doi:10.1038/s41578-019-0169-1

Holmgren, R. T., Tisell, A., Warntjes, M. J. B., and Georgiopoulos, C. (2025). 3D quantitative MRI: a fast and reliable method for ventricular volumetry. *World Neurosurg.* 195, 123661. doi:10.1016/j.wneu.2025.123661

Hostettler, A., George, D., Remond, Y., Nicolau, S. A., Soler, L., and Marescaux, J. (2010). Bulk modulus and volume variation measurement of the liver and the kidneys *in vivo* using abdominal kinetics during free breathing. *Comput. methods programs Biomed.* 100 (2), 149–157. doi:10.1016/j.cmpb.2010.03.003

Hu, C., Wang, L., Liu, S., Sheng, X., and Yin, L. (2024). Recent development of implantable chemical sensors utilizing flexible and biodegradable materials for biomedical applications. *ACS Nano* 18 (5), 3969–3995. doi:10.1021/acsnano.3c11832

Huang, X., Liu, Y., Hwang, S. W., Kang, S. K., Patnaik, D., Cortes, J. F., et al. (2014). Biodegradable materials for multilayer transient printed circuit boards. *Adv. Mater.* 26 (43), 7371–7377. doi:10.1002/adma.201403164

Hwang, S. W., Kang, S. K., Huang, X., Brenckle, M. A., Omenetto, F. G., and Rogers, J. A. (2015). Materials for programmed, functional transformation in transient electronic systems. *Adv. Mater.* 27 (1), 47–52. doi:10.1002/adma.201403051

Ikar, M., Grobecker-Karl, T., Karl, M., and Steiner, C. (2020). Mechanical stress during implant surgery and its effects on marginal bone: a literature review. *Quintessence Int.* 51 (2), 142–150. doi:10.3290/j.qi.a43664

Jacobs, T. S., Won, J., Graveraux, E. C., Faries, P. L., Morrissey, N., Teodorescu, V. J., et al. (2003). Mechanical failure of prosthetic human implants: a 10-year experience with aortic stent graft devices. *J. Vasc. Surg.* 37 (1), 16–26. doi:10.1067/mva.2003.58

Johnson, M. W., Peckham, P. H., Bhadra, N., Kilgore, K. L., Gazdik, M. M., Keith, M. W., et al. (1999). Implantable transducer for two-degree of freedom joint angle sensing. *IEEE Trans. Rehabil. Eng.* 7 (3), 349–359. doi:10.1109/86.788471

Kang, H. S., Kim, S., Song, H., Lee, Y., Jang, J., Chung, W. G., et al. (2025). Skin-tailored adhesive bio-electrode with tunable Poisson's ratio for stable electrophysiological communication. *Adv. Healthc. Mater.* 14 (10), 2404882. doi:10.1002/adhm.202404882

Kang, S. K., Murphy, R. K., Hwang, S. W., Lee, S. M., Harburg, D. V., Krueger, N. A., et al. (2016). Bioresorbable silicon electronic sensors for the brain. *Nature* 530 (7588), 71–76. doi:10.1038/nature16492

Kang, S. K., Park, G., Kim, K., Hwang, S. W., Cheng, H., Shin, J., et al. (2015). Dissolution chemistry and biocompatibility of silicon- and germanium-based semiconductors for transient electronics. *ACS Appl. Mater Interfaces* 7 (17), 9297–9305. doi:10.1021/acsami.5b02526

Kim, B. J., Shin, H. A. S., Jung, S. Y., Cho, Y., Kraft, O., Choi, I. S., et al. (2013). Crack nucleation during mechanical fatigue in thin metal films on flexible substrates. *Acta Mater.* 61 (9), 3473–3481. doi:10.1016/j.actamat.2013.02.041

Kim, C.-W., Kim, G. W., and Kang, G. G. (2024). Practical measures of three-dimensional stretchability on stretchable displays. *J. Inf. Disp.* 25 (2), 169–177. doi:10.1080/15980316.2023.2242596

Kim, J. C., Lee, M., and Yeo, I.-S. L. (2022). Three interfaces of the dental implant system and their clinical effects on hard and soft tissues. *Mater. horizons* 9 (5), 1387–1411. doi:10.1039/d1mh01621k

Kim, S., Oh, Y. S., Lee, K., Kim, S., Maeng, W. Y., Kim, K. S., et al. (2023). Battery-Free, wireless, cuff-Type, multimodal physical sensor for continuous temperature and strain monitoring of nerve. *Small* 19 (32), e2206839. doi:10.1002/smll.202206839

Koo, J., MacEwan, M. R., Kang, S. K., Won, S. M., Stephen, M., Gamble, P., et al. (2018). Wireless bioresorbable electronic system enables sustained nonpharmacological neuroregenerative therapy. *Nat. Med.* 24 (12), 1830–1836. doi:10.1038/s41591-018-0196-2

Kozai, T. D., Catt, K., Li, X., Gugel, Z. V., Olafsson, V. T., Vazquez, A. L., et al. (2015). Mechanical failure modes of chronically implanted planar silicon-based neural probes for laminar recording. *Biomaterials* 37, 25–39. doi:10.1016/j.biomaterials.2014.10.040

Ledet, E. H., D'Lima, D., Westerhoff, P., Szivek, J. A., Wachs, R. A., and Bergmann, G. (2012). Implantable sensor technology: from research to clinical practice. *JAAOS-Journal Am. Acad. Orthop. Surg.* 20 (6), 383–392. doi:10.5435/JAAOS-20-06-383

Lee, G., Ray, E., Yoon, H. J., Genovese, S., Choi, Y. S., Lee, M. K., et al. (2022). A bioresorbable peripheral nerve stimulator for electronic pain block. *Sci. Adv.* 8 (40), eabp9169. doi:10.1126/sciadv.abp9169

Lee, J., Cho, H. R., Cha, G. D., Seo, H., Lee, S., Park, C. K., et al. (2019). Flexible, sticky, and biodegradable wireless device for drug delivery to brain tumors. *Nat. Commun.* 10 (1), 5205. doi:10.1038/s41467-019-13198-y

Lee, J. H., Jang, T. M., Shin, J. W., Lim, B. H., Rajaram, K., Han, W. B., et al. (2023). Wireless, fully implantable and expandable electronic system for bidirectional electrical neuromodulation of the urinary bladder. *ACS Nano* 17 (9), 8511–8520. doi:10.1021/acsnano.3c00755

Leucht, P., Kim, J. B., Wazen, R., Currey, J. A., Nanci, A., Brunski, J. B., et al. (2007). Effect of mechanical stimuli on skeletal regeneration around implants. *Bone* 40 (4), 919–930. doi:10.1016/j.bone.2006.10.027

Liu, Y., Liu, Z., Zhou, Y., and Tian, Y. (2023). Implantable electrochemical sensors for brain research. *JACS Au* 3 (6), 1572–1582. doi:10.1021/jacsau.3c00200

Lu, D., Liu, T. L., Chang, J. K., Peng, D., Zhang, Y., Shin, J., et al. (2019). Transient light-emitting diodes constructed from semiconductors and transparent conductors that biodegrade under physiological conditions. *Adv. Mater.* 31 (42), 1902739. doi:10.1002/adma.201902739

Maeng, W. Y., Tseng, W. L., Li, S., Koo, J., and Hsueh, Y. Y. (2022). Electroceuticals for peripheral nerve regeneration. *Biofabrication* 14 (4), 042002. doi:10.1088/1758-5090/ac8baa

Majerus, S. J., Fletter, P. C., Ferry, E. K., Zhu, H., Gustafson, K. J., and Damaser, M. S. (2017). Suburothelial bladder contraction detection with implanted pressure sensor. *PloS one* 12 (1), e0168375. doi:10.1371/journal.pone.0168375

Markodimitraki, L. M., Ten Harkel, T. C., Bleys, R., Stegeman, I., and Thomeer, H. (2022). Cochlear implant positioning and fixation using 3D-printed patient specific surgical guides; a cadaveric study. *PLoS One* 17 (7), e0270517. doi:10.1371/journal.pone.0270517

Maron, B. J., Spirito, P., Shen, W.-K., Haas, T. S., Formisano, F., Link, M. S., et al. (2007). Implantable cardioverter-defibrillators and prevention of sudden cardiac death in hypertrophic cardiomyopathy. *Jama* 298 (4), 405–412. doi:10.1001/jama.298.4.405

Miyawaki, S., Choi, S., Hoffman, E. A., and Lin, C. L. (2016). A 4DCT imaging-based breathing lung model with relative hysteresis. *J. Comput. Phys.* 326, 76–90. doi:10.1016/j.jcp.2016.08.039

Mohammed, M. M. (2024). Fundamental drivers of metal fatigue failure and performance, 1, 49, 61. doi:10.62184/mmc.jmmc110020245

Morikawa, Y., Yamagiwa, S., Sawahata, H., Numano, R., Koida, K., and Kawano, T. (2019). Donut-shaped stretchable kirigami: enabling electronics to integrate with the deformable muscle. *Adv. Healthc. Mater.* 8 (23), 1900939. doi:10.1002/adhm.201900939

Nag, D. S., Sahu, S., Swain, A., and Kant, S. (2019). Intracranial pressure monitoring: gold standard and recent innovations. *World J. Clin. cases* 7 (13), 1535–1553. doi:10.12998/wjcc.v7.i13.1535

Ni, X. H., Teng, X. C., Jiang, W., Zhang, Y., and Ren, X. (2024). Multi-objective optimization and theoretical analysis of re-entrant structure with enhanced mechanical properties. *Thin-Walled Struct.* 199, 111791. doi:10.1016/j.tws.2024.111791

Okumura, T., Takahashi, R., Hagita, K., King, D. R., and Gong, J. P. (2021). Improving the strength and toughness of macroscale double networks by exploiting Poisson's ratio mismatch. *Sci. Rep.* 11 (1), 13280. doi:10.1038/s41598-021-92773-0

Park, Y. J., Ryu, Y. I., Choi, M. K., Kim, K. S., and Kang, S. K. (2024). Controlling the lifetime of biodegradable electronics: from dissolution kinetics to trigger acceleration. *Soft Sci.* 4 (3), N/A. doi:10.20517/ss.2024.06

Plathow, C., Ley, S., Fink, C., Puderbach, M., Heilmann, M., Zuna, I., et al. (2004). Evaluation of chest motion and volumetry during the breathing cycle by dynamic MRI in healthy subjects: comparison with pulmonary function tests. *Investig. Radiol.* 39 (4), 202–209. doi:10.1097/01.rli.0000113795.93565.c3

Qian, L., and Zhao, H. (2018). Nanoindentation of soft biological materials. *Micromachines (Basel)* 9 (12), 654. doi:10.3390/mi9120654

Redlich, C., Quadbeck, P., Thieme, M., and Kieback, B. (2020). Molybdenum – a biodegradable implant material for structural applications? *Acta Biomater.* 104, 241–251. doi:10.1016/j.actbio.2019.12.031

Redlich, C., Schauer, A., Scheibler, J., Poehle, G., Barthel, P., Maennel, A., et al. (2021). *In vitro* degradation behavior and biocompatibility of bioresorbable molybdenum. *Metals* 11 (5), 761. doi:10.3390/met11050761

Riccabona, M., Fritz, G. A., Schollnast, H., Schwarz, T., Deutschmann, M. J., and Mache, C. J. (2005). Hydronephrotic kidney: pediatric three-dimensional US for relative renal size assessment--initial experience. *Radiology* 236 (1), 276–283. doi:10.1148/radiol.2361040158

Schulthess, J. L., Spencer, B. W., Petersen, P. G., Woolstenhulme, N. E., Ban, D., Frazer, D., et al. (2023). Experimental results of conductive inserts to reduce nuclear fuel temperature during nuclear volumetric heating. *J. Nucl. Mater.* 574, 154176. doi:10.1016/j.jnucmat.2022.154176

Shin, J., Yan, Y., Bai, W., Xue, Y., Gamble, P., Tian, L., et al. (2019). Bioresorbable pressure sensors protected with thermally grown silicon dioxide for the monitoring of chronic diseases and healing processes. *Nat. Biomed. Eng.* 3 (1), 37–46. doi:10.1038/s41551-018-0300-4

Su, Y., Ping, X., Yu, K. J., Lee, J. W., Fan, J. A., Wang, B., et al. (2017). In-plane deformation mechanics for highly stretchable electronics. *Adv. Mater.* 29 (8), 1604989. doi:10.1002/adma.201604989

Swift, A. J., Woodhouse, N., Fichele, S., Siedel, J., Mills, G. H., van Beek, E. J., et al. (2007). Rapid lung volumetry using ultrafast dynamic magnetic resonance imaging during forced vital capacity maneuver: correlation with spirometry. *Investig. Radiol.* 42 (1), 37–41. doi:10.1097/01.rli.0000250735.92266.6b

Tsang, M., Armutlulu, A., Martinez, A. W., Allen, S. A. B., and Allen, M. G. (2015). Biodegradable magnesium/iron batteries with polycaprolactone encapsulation: a microfabricated power source for transient implantable devices. *Microsystems and Nanoeng.* 1 (1), 15024–10. doi:10.1038/micronano.2015.24

Walley, K. C., Hofmann, K. J., Velasco, B. T., and Kwon, J. Y. (2017). Removal of hardware after syndesmotic screw fixation: a systematic literature review. *Foot and ankle specialist* 10 (3), 252–257. doi:10.1177/1938640016685153

Wang, L. Z., Ding, X. L., Feng, W. T., Gao, Y. M., Zhao, S. D., and Fan, Y. B. (2021). Biomechanical study on implantable and interventional medical devices. *Acta Mech. Sin.* 37 (6), 875–894. doi:10.1007/s10409-021-01116-9

Wang, Q., Chen, Y., Ding, H., Cai, Y., Yuan, X., Lv, J., et al. (2025). Optogenetic activation of mechanical nociceptions to enhance implant osseointegration. *Nat. Commun.* 16 (1), 3093. doi:10.1038/s41467-025-58336-x

Wang, Y., Yang, X., Zhang, X., Wang, Y., and Pei, W. (2023). Implantable intracortical microelectrodes: reviewing the present with a focus on the future. *Microsystems and Nanoeng.* 9 (1), 7. doi:10.1038/s41378-022-00451-6

Wang, Y. C., Chang, D., Zhang, S. J., Wang, Q., and Ju, S. (2019). The accuracy of renal function measurements in obstructive hydronephrosis using dynamic contrast-enhanced MR renography. *Am. J. Roentgenol.* 213 (4), 859–866. doi:10.2214/AJR.19.21224

Xia, H., Meng, J., Liu, J., Ao, X., Lin, S., and Yang, Y. (2022). Evaluation of the equivalent mechanical properties of lattice structures based on the finite element method. *Mater. (Basel)* 15 (9), 2993. doi:10.3390/ma15092993

Yin, L., Cheng, H. Y., Mao, S. M., Haasch, R., Liu, Y. H., Xie, X., et al. (2014). Dissolvable metals for transient electronics. *Adv. Funct. Mater.* 24 (5), 645–658. doi:10. 1002/adfm.201301847

Zhang, X., Medow, J. E., Iskandar, B. J., Wang, F., Shokoueinejad, M., Koueik, J., et al. (2017). Invasive and noninvasive means of measuring intracranial pressure: a review. *Physiol. Meas.* 38 (8), R143–R182. doi:10.1088/1361-6579/aa7256

Zhang, Y., Rytkin, E., Zeng, L., Kim, J. U., Tang, L., Zhang, H., et al. (2025). Millimetre-scale bioresorbable optoelectronic systems for electrotherapy. *Nature* 640 (8057), 77–86. doi:10.1038/s41586-025-08726-4

Zhong, J. L., Zhao, C. F., Liu, Y. Z., Ren, J., Yang, C. H., and Zhang, Z. D. (2024). Meta-materials of re-entrant negative Poisson's ratio structures made from fiber-reinforced plastics: a short review. *Fibers Polym.* 25 (2), 395–406. doi:10.1007/s12221-023-00455-7